

# Precision Millimeter-Wave-Modulated Wideband Source at 92.4 GHz as a Step Toward an Over-the-Air Reference

Paritosh Manurkar<sup>ID</sup>, Robert D. Horansky, *Member, IEEE*, Benjamin F. Jamroz, Jeffrey A. Jargon<sup>ID</sup>, *Senior Member, IEEE*, Dylan F. Williams<sup>ID</sup>, *Fellow, IEEE*, and Kate A. Remley<sup>ID</sup>, *Fellow, IEEE*

**Abstract**—As the next-generation communications technology continues to evolve to utilize millimeter-wave frequencies, calibration methods are needed for the nonidealities related to these frequencies in communications electronics. In this article, we demonstrate a 1-GHz bandwidth, 64-quadrature-amplitude-modulated signal source at 92.4-GHz carrier frequency with relative phase and magnitude that may be made traceable to primary standards. By using predistortion techniques, we are able to repeatedly obtain a nominal error vector magnitude (EVM) of 1.4%. In addition, we track correlated and uncorrelated uncertainties using a Monte Carlo method to show the distribution of uncertainty of the EVM measurement with the 5th and 95th percentiles at 1.5% and 3.1%, respectively. We examine the dependence of the EVM in the traceable source on digital-to-analog converters’ imbalance and system drift over time. Finally, we use the stable, low-EVM signal to ascertain EVM degradation on- and off-axis in a stationary over-the-air setup.

**Index Terms**—Digitally modulated signal, millimeter-wave wireless communications, over-the-air (OTA) measurements, predistortion, traceability, uncertainty analysis, wireless systems.

## I. INTRODUCTION

MULTIPLE frequency bands between 3 and 100 GHz are being experimented with for the development of millimeter-wave technology [1]–[5] with the current focus on frequency range 1 (410 MHz–7.125 GHz) and frequency range 2 (24.25–52.6 GHz) as defined by the telecommunications standard development organization, 3rd Generation Partnership Project (3GPP) [6], [7]. The impact of these advancements on cellular technology is becoming undeniable with advantages such as increased bandwidths (BWs) and faster data rates. At the same time, the millimeter-wave frequencies will allow low-latency applications that will expand the field

Manuscript received November 14, 2019; revised January 10, 2020 and February 13, 2020; accepted February 19, 2020. Date of publication April 22, 2020; date of current version July 1, 2020. (*Corresponding author: Paritosh Manurkar.*)

Paritosh Manurkar is with the Department of Physics, University of Colorado at Boulder, Boulder, CO 80309 USA, and also with the National Institute of Standards and Technology, Boulder, CO 80305 USA (e-mail: paritosh.manurkar@nist.gov).

Robert D. Horansky, Benjamin F. Jamroz, Jeffrey A. Jargon, Dylan F. Williams, and Kate A. Remley are with the National Institute of Standards and Technology, Boulder, CO 80305 USA (e-mail: robert.horansky@nist.gov; benjamin.jamroz@nist.gov; jeffrey.jargon@nist.gov; dylan.williams@nist.gov; kate.remley@nist.gov).

Color versions of one or more of the figures in this article are available online at <http://ieeexplore.ieee.org>.

Digital Object Identifier 10.1109/TMTT.2020.2983144

of Internet of Things (IoT) [8] to smart manufacturing [9] and real-time control of smart devices interconnected via IoT [10]. It will also enable other smart device technologies such as self-driving cars [11].

However, technology development in the millimeter-wave frequency bands is anything but trivial. There are inherent challenges related to the use of complex modulation schemes, such as orthogonal frequency-division multiplexing (OFDM) and  $m$ -quadrature-amplitude modulation ( $m$ -QAM where  $m \geq 64$ ) and obtaining large-channel BWs on the order of GHz. In addition, it is known that higher frequencies are limited in propagation distances [12]. In order to overcome high path losses at millimeter-wave frequencies, high-gain beam-steering antenna arrays are often necessary. These are characterized using over-the-air (OTA) tests since the use of cables would be incompatible and cumbersome with such arrays [13].

A key component for verifying OTA tests and calibrating receivers is the development of calibrated signal sources. Compared to the hardware in the sub-3-GHz frequencies, millimeter-wave sources typically exhibit greater nonlinear behavior and distortion, making the measurements challenging. The nonlinear behavior and distortion are caused by components such as amplifiers, frequency converters, and the high-speed digital-to-analog converters (DACs).

We have previously demonstrated a wideband, traceable modulated-signal source at 44 GHz with low error vector magnitude (EVM) and uncertainties on the EVM [14]. However, there is significant interest in exploring higher bands such as those comprising the 71–76-, 81–86-, and 92–95-GHz frequencies [15], [16]. We target the highest frequencies in this allocated spectrum, where the hardware is the least ideal, to design a low-distortion, wideband, traceable, precision millimeter-wave modulated-signal source with the goal to demonstrate reliable experimentation and characterization in the 92–95-GHz band. Following the system design, we also make sure that modulated-signal sources at different frequencies can be created by choosing similar hardware components at the said frequencies.

Nonidealities associated with the signal generation and measurement in the 92–95-GHz band compared to the previously demonstrated 44-GHz source include increased noise floor of instrumentation, reduced accuracy in timing-pulse edges due to jitter, repeatability of cables and connectors, temperature and

other environmental effects, instrumentation drift, greater mismatch, and increased impact on EVM if correlations between components of uncertainty are not preserved. We address these nonidealities by applying various corrections during the measurement or postprocessing. The increased noise floor of instrumentation, reduced timing accuracy, and instrumentation drift become critical especially while performing OTA measurements. We perform higher averaging to overcome these issues. We demonstrate that the correction techniques employed previously still hold in the higher frequency band. We correct our calculations for timebase distortion [17], compensate for the repeatability of cables and connectors by performing cable bending measurements [14], correct for reflections due to mismatch and internal oscilloscope impulse response [18], and then apply sequential predistortion [19] to the measured waveforms that corrects for the system nonidealities.

Here, we describe the design of the source such that it can be calibrated to produce signals with low nominal EVM (<1.5%) even after traveling through air. A low EVM signal is desired to characterize vector receivers. Once we obtain this signal, we calculate the uncertainty associated with the EVM values by the use of the NIST Microwave Uncertainty Framework [20] in both conducted and OTA scenarios. We also make sure to preserve the correlations between various components of uncertainty in the Microwave Uncertainty Framework since it ensures reduced EVM and the associated uncertainty [21]. An unpublished extension of [21] also shows that the impact of correlations between uncertainty components on EVM is larger at higher frequencies (increase of 0.46% at 92.4 GHz versus 0.08% at 44 GHz).

Such a well-calibrated modulated-signal source with demonstrably low EVM has practical applications. The practices followed in this demonstration offer a practical method for National Metrology Institutes and other laboratories worldwide for determination of uncertainty in the measurement-based calculation of EVM of modulated signals. The source may also be used for OTA characterization and traceable measurements in spatial channels [22].

## II. EXPERIMENTAL METHODOLOGY

The experimental methodology for the modulated-signal source can be divided into four main blocks, as shown in Fig. 1. Each block possesses a main component, which drives a specific task. The reference-signal-generation (A) is based on a signal generator (SigGen), the modulated-signal generation (B) has the arbitrary waveform generator (AWG), and the traceable measurements are performed on a calibrated equivalent-time sampling oscilloscope (C) with EVM as the output parameter, followed by uncertainty analysis (D) using the NIST Microwave Uncertainty Framework. These functions are explained further in detail in Sections II-A–II-D.

### A. Reference-Signal Generation

The reference-signal generation, marked as **A.** in Fig. 1, consists mainly of a signal generator, which produces a tone at 11 GHz in our case. This sinusoid provides the external

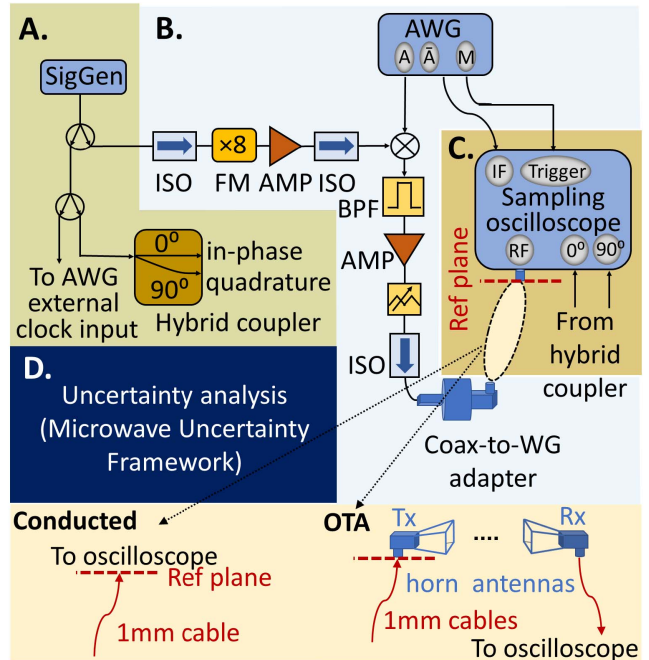


Fig. 1. Schematic of the modulated-signal source at 92.4 GHz. The schematic is divided into four blocks, where each block performs a specific task. **A.** The reference-signal-generation block produces timing signals and an LO for the signal source. **B.** The modulated-signal-generation block produces the signal at 4.4 GHz, which is mixed with the frequency-multiplied LO at 88 GHz to produce the upconverted 92.4-GHz RF signal. **C.** This block measures the RF signal in two configurations, namely, conducted where the source’s output is measured via a 1-mm cable, or, OTA where we connect the 1-mm cable to a transmit horn antenna (Tx) and measure the RF signal by the receive horn antenna (Rx) on the equivalent-time sampling oscilloscope. We use EVM as the output quality parameter. **D.** This block performs the uncertainty analysis on the measured data using the NIST Microwave Uncertainty Framework [20]. (SigGen: signal generator, ISO: isolator, FM: frequency multiplier, AMP: amplifier, BPF: bandpass filter, AWG: arbitrary waveform generator,  $A/\bar{A}$ : interleaved analog outputs,  $M$ : marker output for trigger, IF: measurement port for IF waveform and RF: measurement port for RF waveform.)

clock input for the AWG, which, in turn, triggers the sampling oscilloscope. Using the internal clocks of the equipment does not provide the timing accuracy necessary for a low-phase distortion signal. The 11-GHz clock signal also acts as the local oscillator (LO) for the upconversion process. We use a hybrid coupler to create in-phase and quadrature components of the sinusoid, which are then used to correct the time-base of the equivalent-time sampling oscilloscope. Essentially, the reference-signal-generation block produces all the timing signals required for the modulated-signal source.

### B. Modulated-Signal Generation

The modulated-signal-generation block, marked as **B.** in Fig. 1, deals with everything from numerical calculation of the baseband waveform to actual generation of the modulated signal at 92.4 GHz. The AWG produces two identical but conjugate interleaved analog outputs,  $A$  and  $\bar{A}$ , at the intermediate frequency ( $f_{IF} = 4.4$  GHz), along with the marker output ( $M$ ) used as a trigger for the broadband equivalent-time sampling oscilloscope. The LO frequency ( $f_{LO} = 11$  GHz) is multiplied by a factor of eight and amplified for mixing with the 64-QAM signal from the AWG to produce the RF signal. The RF signal

TABLE I  
WAVEFORM DESIGN PARAMETERS

Parameter	Symbol	Value
Modulation $m$ -QAM	$m$	64
Samples per carrier frequency cycle	$n_s$	5
AWG sampling rate	$f_s$	22 GSamples/s
Intermediate frequency	$f_{IF}$	4.4 GHz
Local oscillator frequency	$f_{LO}$	11 GHz
RF frequency	$f_{RF}$	92.4 GHz
Samples per symbol	$n_{sps}$	20
Symbol rate	$f_{sym}$	1.1 GSymbols/s

is filtered, amplified, and attenuated to an appropriate level for measurement on the sampling oscilloscope. Isolators are used at specific places indicated in Fig. 1 to prevent reflections and ensure directionality. It should be noted that the isolator is the last component in the upconverter chain to ensure good impedance matching with the sampling oscilloscope irrespective of attenuation variation during experimentation.

1) *Waveform Design Parameters:* The signal that we produce here is a special transfer standard meant to be used in the laboratory setting for calibrating other instruments. With this objective in mind, our goal was to design a 64-QAM signal within the various constraints related to the choice of hardware, desired output, and sampling restrictions. The choice of hardware relied completely on commercially available components so that the modulated-signal source can be recreated in any other laboratory.

Here, we provide a guideline on making the choices for various parameters. First, we considered the hardware constraints, namely, a converter with a frequency multiplier of eight to reach the RF filter passband of 92–96 GHz, and an AWG with sampling rate ( $f_s$ ) of up to 24 GSamples/s. We wanted to use as many samples per second as possible while providing an integer number of samples per cycle.

Next, we dealt with the constraints on  $f_{IF}$ . We desired an  $f_{IF}$  high enough to use the widest available modulation BW that could provide at least four samples per RF carrier frequency cycle ( $n_s \geq 4$ ). We also had to make sure that  $f_{IF}$  was such that it avoided interleaved DAC images [23]–[25], that is

$$f_{IF} < f_s/2 - f_{IF} - BW/2. \quad (1)$$

The final constraint was to have an integer ratio of  $f_s$  to the symbol rate  $f_{sym}$ . We chose this ratio as 20 samples/symbol ( $n_{sps} = 20$ ).

Table I summarizes the parameters needed for waveform generation under the discussed constraints.

2) *Symbol Generation:* We initialized the constellation indices for the 64-QAM signal. We then generated a pseudo-random binary sequence (PRBS) using a PRBS-9 algorithm, which gave us the number of bits as  $\mathcal{N} = 2^k - 1 = 511$ , where  $k = 9$ . To create the symbols from the PRBS-9 sequence, we repeated the  $\mathcal{N}$ -element-long random binary signal  $n$  times, where  $n = \log_2(m) = 6$ , for  $m = 64$ , resulting in a bitstream,  $\mathcal{B}$ , with length  $n \times \mathcal{N} = 3066$ . Finally, we combined every  $n$  elements in  $\mathcal{B}$  to form a symbol,  $\mathcal{S}_i$ , where  $i$  is an index

variable going from 1 to 511. The  $i$ th symbol may then be represented as follows:

$$\mathcal{S}_i = \sum_{q=1}^n 2^{(q-1)} \times \mathcal{B}_{q+6(i-1)}. \quad (2)$$

3) *Signal Generation:* We extended the 511 symbols with 30 guard symbols on each end to account for filter causality. Next, we assigned the symbols to the constellation indices followed by gain normalization to produce a normalized modulated signal. We padded this signal with zeros for upsampling to achieve 1.1 GSymbols/s with 22 GSamples/s followed by filtering the padded sequence with a root-raised cosine filter (rolloff = 0.35 and delay = 22 ns) to obtain the signal  $\mathcal{S}_{filtered}$ .

We removed the extra samples due to guard symbols from  $\mathcal{S}_{filtered}$  to produce the baseband signal,  $\mathcal{S}_{baseband}$ . To create the final intermediate-frequency waveform ( $\mathcal{S}_{IF}$ ), we translated  $\mathcal{S}_{baseband}$  to the intermediate frequency by multiplying with a complex carrier ( $\mathcal{S}_{carrier}$ ) and extracting the real part. The complex carrier was defined, as shown in (3), using the carrier frequency of  $f_{IF} = 4.4$  GHz and a time grid ( $t_{grid}$ ) defined by a step size equal to the inverse of the sampling rate

$$\mathcal{S}_{carrier} = \exp(-i \times 2\pi \times f_{IF} \times t_{grid}) \quad (3)$$

$$\mathcal{S}_{IF} = \text{Re}(\mathcal{S}_{baseband} \times \mathcal{S}_{carrier}). \quad (4)$$

We uploaded this waveform consisting of ( $f_s \times \mathcal{N}/f_{sym} =$ ) 10220 points to the AWG. The period of this waveform was calculated as ( $\mathcal{N}/f_{sym} =$ ) 464.5455 ns, or equivalently, a repetition rate of 2.1526 MHz (both rounded to four places after the decimal).

4) *Measurement Parameters:* On the measurement side, we selected a time step of one-eighth of the reciprocal of 92.4 GHz such that each sinusoid period consisted of eight sample points resulting in an integer total number of points per cycle and no partial sinusoidal cycles in the measured waveform. This condition was critical for performing Fourier transform calculations later. This time step resulted in a total of 343392 points in the measured time-domain waveform. Given the time-domain properties of the waveform and using the maximum number of points available in an equivalent-time sampling oscilloscope frame (16384), we measured 21 frames in order to record the entire length of the modulated signal. We performed 25 such measurements for time-domain averaging [17] to reduce noise in the oscilloscope measurements. We chose 25 measurements for averaging because it provided a low nominal EVM without a significant increase in postprocessing time. Table II shows these values for a fourth predistortion measurement data set.

### C. Conducted and OTA Measurements

We performed both conducted and OTA measurements using the calibrated equivalent-time sampling oscilloscope. The oscilloscope head had a BW of 67 GHz, which means that we were using it outside its single-mode range. We will be exploring a higher BW oscilloscope head in the future.

Fig. 2 shows a photograph of our precision modulated-signal source at 92.4 GHz highlighting the signal generator, AWG, the equivalent-time sampling oscilloscope, the reference plane,

TABLE II  
NOMINAL EVM VERSUS POSTPROCESSING TIMES

Averages	Nominal EVM (%)	Post-processing times (min)
5	2.10	5.6
10	1.65	8.6
15	1.54	11.4
20	1.46	15.0
25	1.42	18.3

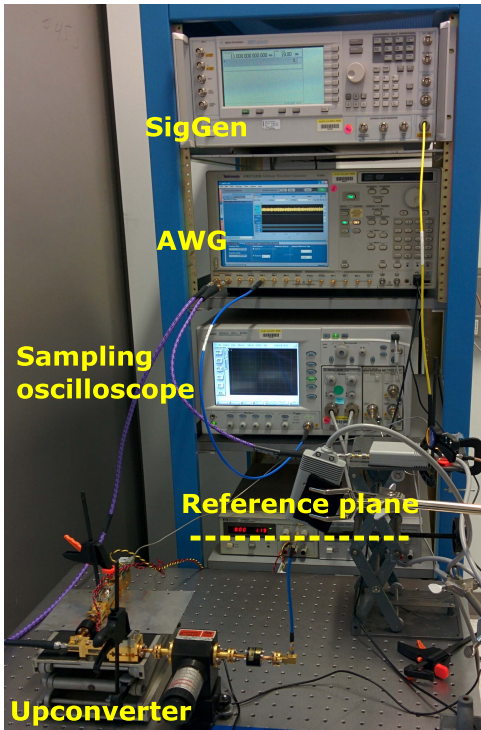


Fig. 2. Setup shows the signal generator (SigGen), AWG, the calibrated sampling oscilloscope, the upconverter, and the source’s output reference plane at the end of the 1-mm coaxial connector. We upload the predistorted spectrum to the AWG such that it creates the desired signal spectrum at the reference plane.

and the upconverter consisting of multiplier, mixer, isolators, and amplifiers.

The measurements made on the equivalent-time sampling oscilloscope—whether conducted or OTA—required several corrections for accurate characterization of the output signal of the modulated-signal source. First, we performed timebase, mismatch, and oscilloscope response corrections on the measured data irrespective of whether the data were measured with or without DAC imbalance corrections. Then, we performed predistortion calculations to account of the remaining hardware nonidealities in the system.

1) *Timebase, Mismatch, and Oscilloscope Response Corrections:* First, we applied corrections for jitter and systematic errors in the oscilloscope’s timebase. These corrections were achieved by the use of algorithms [17], [26] that estimate a new timebase for the measured data. The hybrid coupler’s in-phase and quadrature outputs provided references for the calculation of the new timebase.

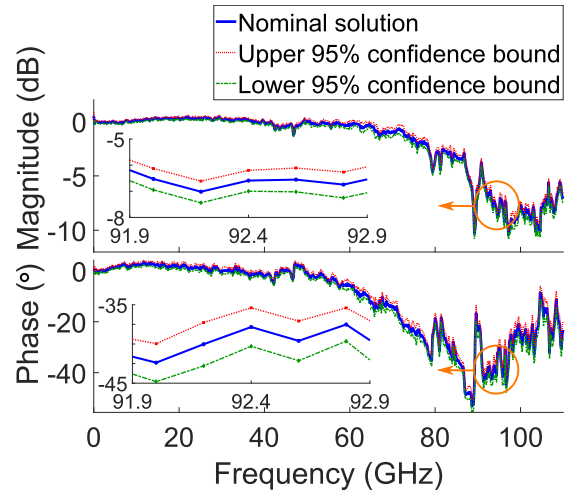


Fig. 3. Measured magnitude and phase responses of the 67-GHz oscilloscope head along with the 95% confidence bounds. The insets in each subplot show the magnitude and phase responses in a 1-GHz BW around the RF frequency of 92.4 GHz.

We also applied drift correction to align the 25 oscilloscope measurements in time. The drift is usually caused by trigger delays in one measurement relative to the other. This process was based on a previously demonstrated method of time-to-frequency domain conversion followed by phase detrending of frequency components within a narrow BW around the carrier frequency [27]. We assigned the first measured signal as the reference and time-aligned all the other measurements to the said reference.

Next, we performed time-domain averaging of the timebase- and drift-corrected waveforms. The timebase correction created waveforms with an irregular spaced grid of time points. We employed a more accurate method than simply interpolating and averaging the 25 measurements. We extracted all of the voltage values around a time point from all the 25 measurements and then performed a curve fitting step to calculate the voltage value for the required time point [28]. Repeating this calculation for each time step in the waveform, we obtained a signal which could then be Fourier-transformed into the frequency domain where corrections related to the internal oscilloscope response and impedance mismatch between the oscilloscope and the source could be performed. Using the uncertainty framework described below, these corrections provide the traceability path for the measurement [18], [29].

Fig. 3 shows the magnitude and phase responses of the oscilloscope to a calibrated photodiode input along with the 95% confidence bounds. The insets of each graph show the magnified frequency scale relevant to the measurements presented here. The oscilloscope response must be interpolated to correct for the frequency grid used in the current measurements, but we assumed that the uncertainties derived at each 200-MHz frequency point are large enough to encompass the uncertainty in the modulated signal’s frequency components in both magnitude and phase.

2) *DAC Imbalance Corrections:* In our previous studies, it was noted that DAC imbalance corrections were critical [30]

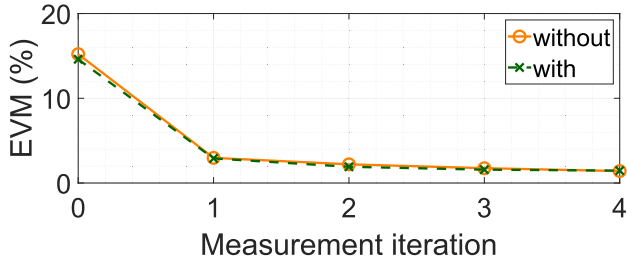


Fig. 4. Effect of DAC imbalance correction on measured nominal EVM values after predistortion. We measured the EVM without (orange) and with (green) application of DAC imbalance correction. For both cases, we also predistorted the measured signal four times. It is evident from the plotted data that DAC imbalance does not have a significant effect on measurement at 92.4 GHz. The zeroth measurement iteration refers to the original measurement while the next measurements refer to the  $i$ th predistortion, where “ $i$ ” is the respective iteration.

since we interleave the DAC outputs to achieve higher AWG sampling rates. We performed the DAC imbalance measurement for this modulated source as well. The goal of performing these measurements was to compute the individual frequency responses of the two DACs. We enabled only the first DAC output by programming every even data point on the uploaded waveform to zero followed by performing oscilloscope measurements, timebase corrections, and other postprocessing methods as described before. We repeated the same procedure for the second DAC output, but this time, every odd data point was set to zero. We then compared the two frequency responses within the center BW relative to  $f_{IF}$  and computed the complex imbalance between the two spectral data. We subsequently applied a prefilter to the waveform uploaded to the second DAC to compensate for the imbalance in its frequency response relative to the first DAC [30].

We found that the DAC magnitude imbalance for the 92.4-GHz source was significantly lower than that shown in [30]. On the other hand, the DAC phase imbalance was similar. The difference in magnitude imbalance can perhaps be attributed to factors such as environmental stability of the laboratory space between the two DAC imbalance measurements. The work on the 92.4-GHz source was done in a well-controlled environment with respect to temperature and relative humidity. Temperature and relative humidity measurements from near the setup but from a different week suggest 1 °C variation in temperature and 5% variation in relative humidity. These variations are much better than the previous variations when there was no temperature and relative humidity control. Reference [31] provides an example of the effect of temperature drift on the performance of precision DACs. It is safe to infer that any imbalance would have been compounded due to relative drifts between two interleaving DACs in our previous work [14], [30].

To ascertain the extent of DAC imbalance at 92.4 GHz, we also performed predistortion measurements without DAC imbalance corrections. Fig. 4 shows that the EVM values without and with DAC imbalance corrections were quite similar. This outcome along with the difference between the DAC magnitude imbalances for the two sources implied that the DAC imbalance coefficients at 92.4 GHz were not as

critical as they were at 44 GHz. Anyhow, we have kept the DAC imbalance correction as part of the workflow for all the data shown in this article, but its importance at 92.4 GHz seems to be minimal.

3) *Predistortion*: Performing the corrections described above gave us a waveform measured on the oscilloscope primarily limited by the nonidealities of the physical hardware of the modulated-signal source. To account for these nonidealities, we predistorted the signal and uploaded the predistorted signal to the AWG. Predistortion reduces the nonideal behavior of the hardware components and produces an improved waveform at the reference plane, as described in [19].

To calculate the predistorted signal, we compared the original multisine signal (corresponding to the original uploaded time-domain signal on the AWG) with the measured multisine signal (corresponding to the measured time-domain signal), both of which were computed using 845 components and a repetition rate of 2.1526 MHz as obtained in Section II-B3. Multisine signals are a class of periodic test signals consisting of a sum of several sinusoids. They are often used in wireless metrology because they are periodic and, thus, relatively easy to measure yet they can be made statistically similar to digitally modulated signals [32]. In these predistortion calculations, we employed three different BWs, namely, measured BW, processing BW, and detrending BW. The measured BW is  $df = 2.1526$  MHz multiplied by the total number of components (845) in the multisine. This includes the signal + filter rolloff. We effectively applied a “brick-wall” filter by using a processing BW for computing the predistortion coefficients given by the 639 frequency components around the RF carrier frequency. The detrending BW is obtained by using 93 frequency components centered at the carrier frequency of the multisine such that the phase detrending is performed where the signal power is maximum.

If  $X_{in,ideal}(f)$  and  $Y_{out}(f)$  are the ideal input and the distorted output, respectively, they are related by the source’s frequency response,  $H(f)$ , as follows:

$$Y_{out}(f) = H(f)X_{in,ideal}(f). \quad (5)$$

We can obtain an estimate of the unknown system response, that is, combined source + oscilloscope response with the measured  $Y_{out,meas}(f)$  as follows:

$$H_{est,j}(f) = \frac{Y_{out,meas}(f)}{X_{in,ideal}(f)}. \quad (6)$$

This estimate, in turn, is used to compute a predistorted (abbreviated as PreD for simplification) input,  $X_{in,PreD(j+1)}(f)$ , as follows:

$$X_{in,PreD(j+1)}(f) = \frac{X_{in,ideal}(f)}{H_{est,j}(f)}. \quad (7)$$

The predistorted input  $X_{in,PreD(j+1)}(f)$  is then uploaded on the AWG followed by calculation of the next better estimate of system response,  $H_{est,(j+1)}(f)$ , where  $j$  is incremented each iteration. Subsequently, we obtain a version of predistorted input,  $X_{in,PreD4}(f)$ , which can compensate for the system nonlinearities and distortion and produce a cleaner output.

It should be noted that all of the above quantities are complex and have both magnitude and phase components.

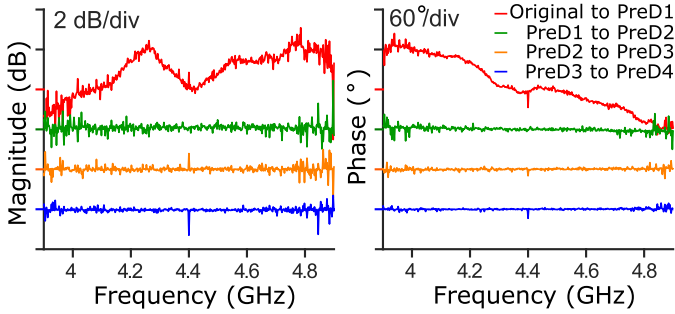


Fig. 5. Magnitude and phase gain obtained by iteratively predistorting the signal uploaded on the AWG to produce a near-ideal spectrum at the reference plane. This graph shows the evolution of the spectrum centered at 4.4 GHz with a BW of 1 GHz with each predistortion. A flat curve denotes similar magnitude and phase information in the previous predistorted spectrum as the current one. The curves have been shifted for better visualization. (PreDi = abbreviation for  $i$ th predistorted spectrum.)

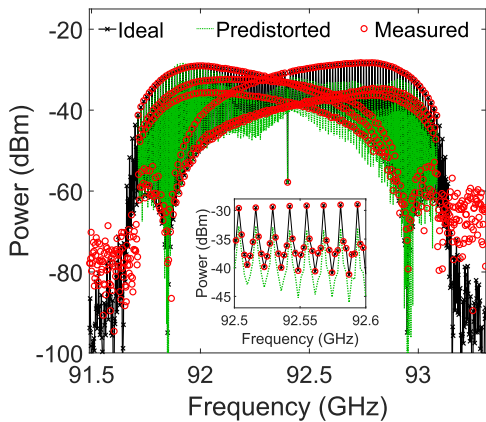


Fig. 6. Spectrum of the 64-QAM signal. The figure shows three spectra of interest translated to 92.4 GHz: the ideal spectrum (black crosses) which is a simulated 64-QAM signal, the predistorted spectrum (green), and the measured spectrum (red circles) at the reference plane after four iterations of predistortion. Inset shows good agreement between the measured and ideal spectra.

To assess the progression of the predistortion technique, we calculated and plotted the magnitude and phase gain for the predistortion sequence, as shown in Fig. 5. The plot shows magnitude and phase gain for a signal having a BW of 1 GHz centered at 4.4 GHz. For better visualization, we define magnitude gain as the ratio of the magnitudes of the two spectra in question converted to decibels and the phase gain as the subtraction of the phases, in degrees, of the two spectra. As expected, these gain profiles became flatter with each predistortion iteration because the difference between the subsequent waveforms became negligible.

The result of the iterative predistortion technique is shown in Fig. 6, where we compare the measured spectrum (red circles) in the conducted case with the calculated predistorted spectrum (green) and the designed ideal signal spectrum (black crosses)—all translated to  $f_{RF} = 92.4$  GHz.

4) *EVM Calculation*: We used commercially available software for EVM calculation of the measured original signal and those produced after each predistortion. The software performs a nondata-aided EVM calculation. Due to restraints imposed

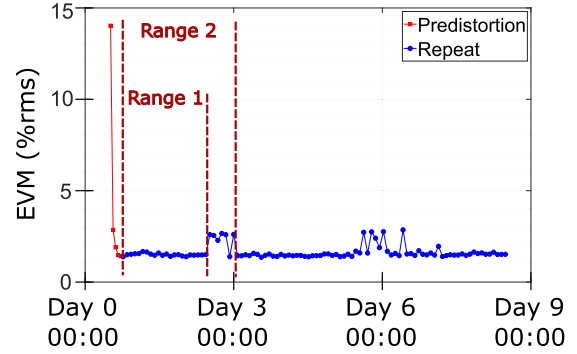


Fig. 7. Nominal EVM values for predistortion measurements (red squares) to obtain a greatly improved spectrum followed by repeat measurements (blue circles) to demonstrate the stability of our modulated-signal source. The automated measurement lasted for a total of nine days.

by the software, it employs 380 symbols for the EVM calculation. It uses a root-raised cosine filter with  $\alpha = 0.35$  as the measurement filter while using a raised cosine as the reference filter. The EVM is normalized to the reference rms and not the constellation maximum. These values are kept consistent with the work in [14] so that the EVM values can be compared directly. In the future, we intend to steer away from the commercially available software and yet maintain traceability by following the IEEE P1765 Best Practice document. The latter describes a Baseline EVM Algorithm that utilizes only the minimum number of steps necessary to compute EVM. Proprietary filtering, time alignment, and sampling techniques are eliminated in this article. The source presented here was designed with this waveform-based EVM calculation in mind.

EVM is a measure of the deviation of the measured signal from the ideal signal and is defined as follows:

$$\text{EVM} = \left[ \frac{\frac{1}{N} \sum_{i=1}^N |\mathcal{S}_{\text{ideal},i} - \mathcal{S}_{\text{meas},i}|^2}{\frac{1}{N} \sum_{i=1}^N |\mathcal{S}_{\text{ideal},i}|^2} \right]^{\frac{1}{2}} \quad (8)$$

where it is normalized relative to the root-mean-squared value [33].  $\mathcal{S}_{\text{ideal},i}$  are the ideal symbols defined in Section II-B2,  $\mathcal{S}_{\text{meas},i}$  are the corresponding measured symbols, and the index variable  $i$  varies from 1 through  $N = 511$ .

Fig. 7 shows the nominal EVM values computed for predistortion (red squares) and stability estimation (blue circles) measurements. The nominal value refers to the estimate of the EVM, which includes the oscilloscope response correction, the mismatch correction, and time corrections. In this measurement, we obtained a nominal EVM of 1.4% after four rounds of predistortion. Furthermore, as evident from the blue data points—separated by approximately 2 h on the  $x$ -axis—the modulated-signal source was stable in the measured EVM for about a week except for two regions of slightly higher values. We call these two data ranges as Range 1 and Range 2 corresponding to their occurrences on Day 2 and Day 5, respectively. The effect of the bumps will be studied in Section II-D. It should be noted though that the modulated-signal source was kept in a controlled laboratory where the room's temperature and relative humidity were monitored centrally in the building. Environmental

monitoring data from proximity of our setup but from a different week showed spikes in the relative humidity data. These spikes may provide a plausible explanation for the bumps as well. Unfortunately, we cannot draw a more concrete conclusion at this time. Readers will find it interesting though that even in a temperature-controlled laboratory, environmental effects can affect measurements at high millimeter-wave bands.

5) *OTA Measurements*: We conducted a preliminary OTA experiment with a predistorted waveform with a nominal EVM of 1.5% to observe the effect on EVM in both on- and off-axis scenarios. We set up two WR10 horn antennas on an optical table with RF absorbers strategically placed around the setup to avoid geometric bounces from the optical table as a means to counter the main source of scattering. In this preliminary demonstrative experiment, we assumed that other reflections were negligible. We disconnected the 1-mm cable at the reference plane and connected it to the transmit (Tx) horn antenna via a coaxial-to-waveguide adapter. On the other side, we connected the receive (Rx) horn antenna to the oscilloscope head via another coaxial-to-waveguide adapter and 1-mm cable. We aligned the two antennas by hand, kept at an approximate distance of 60 cm, to maximize the signal level observed on the oscilloscope. We approximated the separation between the two antennas using the mounting holes on the optical table. A standard optical table has mounting holes separated by 2.54 cm.

As expected, we found that the measured signal strength (21 mV<sub>pp</sub>) was much lower compared to the conducted case due to beam divergence. We computed the expected output signal strength to be measured on the oscilloscope using the Friis transmission equation [12]. The raw oscilloscope trace files measured before disconnecting the 1-mm cable gave us an estimate of the Tx power. The two horn antennas each had a gain of  $\approx 23$  dB at  $f_{RF} = 92.4$  GHz. Given the approximate separation between them (60 cm), we obtained the expected output signal strength as 27 mV<sub>pp</sub>. This approximate 2-dB discrepancy from expectation can be accounted for by mechanisms such as contribution from the coaxial-to-waveguide adapters, reflection of the signal at the apertures of the horn antennas, uncertainty in the defined distance between the antennas, and the rough approximation of the gain of the two antennas from the manufacturer’s datasheet.

Fig. 8(a)–(c) shows the experimental setup employed to measure the corrected 64-QAM signal OTA. We show the setup in the top view so that the alignment between the two antennas can be clearly observed. In Fig. 8(a), the two antennas were aligned to maximize the received signal while in Fig. 8(c), they were kept at an offset of 9°. We transmitted the previously predistorted waveform OTA and measured a nominal EVM of 6.3%. The higher EVM in this case was expected because the predistortion had taken into account only the nonidealities of the conducted setup. Thus, we predistorted the recorded signal after traveling OTA. Interestingly, we obtained a low nominal EVM value of 1.2% after four additional predistortion iterations, as shown in Fig. 8(b). We also performed repeat measurements (blue circles) for the calculation of uncertainty.

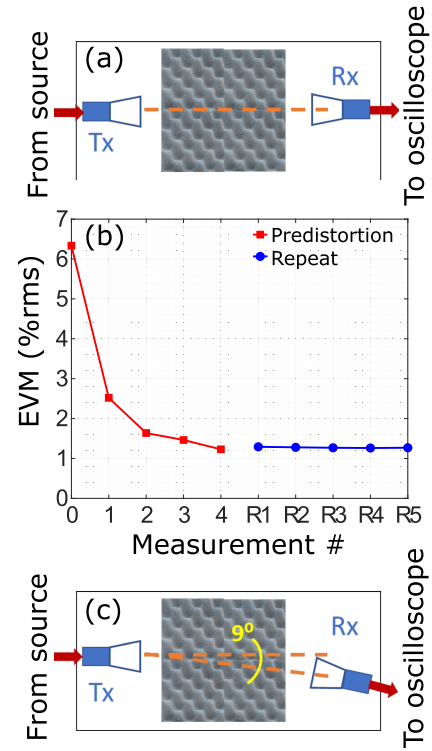


Fig. 8. OTA measurements and predistortion. We connected the RF output at the reference plane to a horn antenna (Tx) which was then received by another horn antenna (Rx) approximately 60 cm away. (a) We aligned the antennas and measured the received signal on the sampling oscilloscope. (b) We predistorted the input signal to improve the waveform at the Rx horn antenna. This graph shows the EVM values for the predistortion (red squares) and repeat measurements (blue circles) to ascertain stability of the waveform. (c) Antennas were kept at an angular offset of 9° to check the degradation of EVM value. The angular offset was computed using the  $X$  and  $Y$  offsets between the two antennas.

Note that these measurements were performed with 100 oscilloscope measurements for each data set versus 25 oscilloscope measurements to better analyze the angular dependence of the EVM. To compare the nominal EVM value obtained using 100 versus 25 oscilloscope measurements, we processed the same data set now using the first 25 oscilloscope measurements. This calculation gave us a nominal EVM value of 1.4%, which is similar to that obtained in the conducted case. However, in Section II-D where we discuss the uncertainty analysis, it can be seen that the increased number of averages does not give rise to better uncertainty estimates.

To study the off-axis behavior, we offset the receiver antenna relative to the source antenna and measured the received waveform again. With an offset of 9°, we recorded a weaker signal on the sampling oscilloscope. The angle offset was calculated based on the  $X$  and  $Y$  offsets between the two antennas estimated again using the mounting holes on the optical table. Following the same data processing techniques mentioned earlier, we computed a nominal EVM of 3.3%. We could potentially obtain a lower EVM value for this case by predistorting the input signal.

Here, we investigate the relationship between EVM and signal-to-noise ratio (SNR) with respect to our experiment. SNR and EVM share an inverse relationship [34], [35], which

can be related to the measured peak-to-peak voltage ( $V_{\text{meas}}$ ) on the sampling oscilloscope for the OTA tests as follows:

$$\text{EVM} \approx \frac{1}{\sqrt{\text{SNR}}} \propto \frac{1}{V_{\text{meas}}}. \quad (9)$$

$V_{\text{meas}}$  for the on-axis case was 21 mV<sub>pp</sub> and that for the off-axis case was 12 mV<sub>pp</sub>. The EVM computed for the on-axis case was 1.2%. Given this information, we computed the expected off-axis nominal EVM to be 2.1%, which is significantly lower than the obtained nominal EVM of 3.3%. This calculation implies that the SNR reduction alone is not sufficient to explain the observed EVM reduction. We need to account for the phase curvature at the Rx horn antenna pattern due to the angular separation between the antennas, which is significant enough to affect the alignment of the antenna [36], thus increasing the measured EVM. The OTA experiments will be expanded to other frequencies in the future. We also plan to perform OTA stability test similar to that shown in Fig. 7 for the conducted case. The purpose of the current OTA test was to demonstrate the usability of our modulated-signal source in performing both on-axis and off-axis measurements along with the application of predistortion techniques and full uncertainty analysis, the latter shown in Section II-D.

#### D. Uncertainty Analysis

We employed the NIST Microwave Uncertainty Framework for estimation of uncertainties by performing repeat measurements of the final predistorted waveform and cascading this distribution with systematic uncertainties from every step of the calibration process. The uncertainty analysis propagates correlations between components of uncertainty in each processing step. In each step, we performed a sensitivity analysis and 1000 Monte Carlo simulations. EVM is calculated using the same software settings as mentioned in Section II-C4 for the calculation of the nominal EVM. However, to create the EVM distribution, the Microwave Uncertainty Framework calls the software for each of the 1000 Monte Carlo perturbed waveforms and computes 1000 EVM values. We performed the uncertainty analysis for the two data ranges as highlighted in Fig. 7. Fig. 9 shows a simple block diagram of the employed uncertainty analysis. Further details can be found in [14].

Briefly, we combined the repeat oscilloscope measurements in the first step to find the random component of uncertainty associated with repeat measurements.

The second step assessed the uncertainties associated with the followings: 1) the bending of the 1-mm cable connecting the output of the modulated-signal source to the oscilloscope; 2) reflection coefficients of the source and the receiver resulting from an impedance mismatch between the source and the equivalent-time sampling oscilloscope; and 3) oscilloscope's internal response [18], [37], [38]. This response was calibrated with the NIST electrooptic sampling system using a photodiode transfer standard. This system provides phase traceability through the primary standards of volt, meter, and second [18], [29], [39]–[41].

In the third step, we transformed the frequency-domain estimates from the previous steps into time-domain representation of the perturbed modulated-signal source output waveforms while preserving the uncertainty correlations.

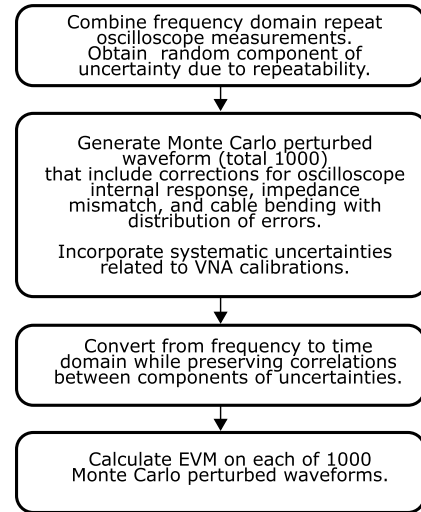


Fig. 9. Block diagram for the uncertainty analysis for the modulated-signal source at 92.4 GHz.

Finally, we computed EVM values from the perturbed time-domain waveforms obtained in the previous step. As a result, we obtained an EVM distribution along with the nominal solution, Monte Carlo estimate, and the Monte Carlo 95% confidence intervals. The nominal value will always be the lowest EVM possible due to the use of predistortion and can be obtained only during the calibration step. The reason for the previous statement and the asymmetric distribution for the uncertainty analysis is that we predistort the waveform based on the knowledge of the estimates for all the correction factors that go into postprocessing and traceability. However, for a given measurement, the value of one of these factors will likely not be the mean estimate, and therefore, the predistortion will no longer minimize the EVM. Thus, the Monte Carlo estimate is the value that is likely obtained during a measurement.

We included oscilloscope calibration errors in our overall uncertainty. The analysis included errors in the NIST electrooptic sampling system that was used to calibrate the impulse response of the photodiode later used to calibrate our oscilloscope. This part of the uncertainty analysis is described in [41]. The oscilloscope calibration uncertainty also included errors in the oscilloscope's timebase corrections, repeatability, and mismatch corrections [18].

Operating the oscilloscope above the cutoff frequency of its 1.85-mm connector can lead to errors in the oscilloscope calibration due to overmoding in the input section of the oscilloscope. This overmoding may cause high- $Q$  resonances that manifest themselves as “suckouts” in the input section of the oscilloscope. These resonances are calibrated out in the calibration process but can be sensitive to small changes in the input section. First, the adapters were chosen to minimize the length of the input section, which is short in the oscilloscope we used, minimizing the sensitivity of the resonances to temperature and other changes. Then, the impulse response of the oscilloscope was characterized multiple times and the differences in the calibrations incorporated into the overall uncertainty budget for the oscilloscope calibration. Correlations were preserved throughout the uncertainty analysis, making the analysis suitable for waveform and modulated-signal metrology [14].

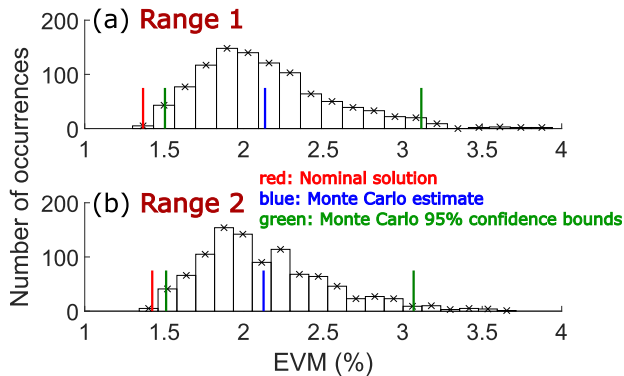


Fig. 10. Uncertainty analysis for the modulated-signal source at 92.4 GHz. (a) Uncertainty analysis for Range 1 where the EVM values remained stable. (b) Uncertainty analysis for Range 2 where the EVM values showed a bump as well. Both the EVM distributions show the nominal solutions (short red lines), the Monte Carlo estimate (short blue lines), and the Monte Carlo 95% confidence bounds (short green lines).

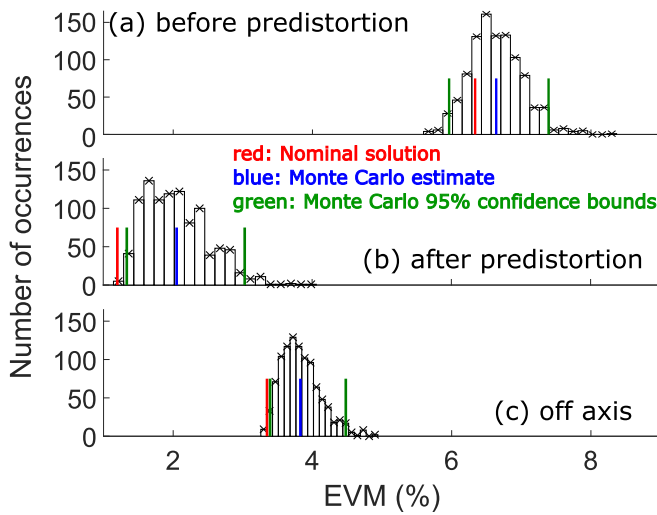


Fig. 11. Uncertainty analysis for the OTA measurements using the modulated-signal source at 92.4 GHz. The three EVM distributions show the nominal solutions (short red lines), the Monte Carlo estimate (short blue lines), and the Monte Carlo 95% confidence intervals (short green lines). (a) Uncertainty analysis for the OTA measurement using the predistorted waveform which had 1.5% nominal EVM at the reference plane. No predistortion was applied OTA at this step. (b) Uncertainty analysis for the OTA measurement using the waveform obtained after predistorting the signal OTA. (c) Uncertainty analysis for the off-axis OTA measurement.

Fig. 10(a) and (b) shows the EVM distributions obtained for the two data ranges shown in Fig. 7. It was expected that the nominal solution for Range 2 would be slightly higher than that for Range 1 simply because the former includes the region with higher EVM values. The nominal EVM values were 1.37% and 1.43% for Range 1 and Range 2, respectively. However, the Monte Carlo estimates (2.13%) were the same for both the ranges because the two measurement sets (ranges) had similar error mechanisms.

We also performed a full uncertainty analysis for the OTA measurements. We studied three cases, namely, the first OTA measurement before predistorting the signal (nominal EVM of 6.3% at Rx), the second OTA measurement after predistorting the input signal to compensate for OTA path (nominal EVM of 1.2% at Rx), and finally, the OTA measurement in the

TABLE III

RESULTS FROM THE UNCERTAINTY ANALYSES FOR THE OTA EXPERIMENT. THE MONTE CARLO ESTIMATE IS THE VALUE THAT IS LIKELY OBTAINED DURING A MEASUREMENT

OTA case	Nominal value	Monte Carlo estimate	Lower 95% bound	Upper 95% bound
Before predistortion	6.3%	6.6%	6.0%	7.4%
After predistortion	1.2%	2.1%	1.3%	3.0%
Off axis	3.3%	3.8%	3.4%	4.5%

off-axis configuration (nominal EVM of 3.3% at Rx). The EVM distributions obtained from these uncertainty analyses are shown in Fig. 11, and a summary of important values is presented in Table III. It should be noted that the predistortion in Table III is referring to the predistortion performed to compensate for the OTA path.

### III. CONCLUSION

In this article, we have demonstrated a precision low-distortion modulated-signal source at a significantly high frequency of 92.4 GHz that can be calibrated to primary standards. We designed a 64-QAM signal as a special transfer standard to calibrate other instruments in the laboratory. The careful design of the signal included subjecting it to several constraints driven by the choice of hardware and experimental parameters. We performed both conducted and OTA measurements after studying DAC-imbalance issues and using the predistortion technique. At the same time, we performed full uncertainty analysis for each case. For the conducted case, we measured a signal with EVM in the 5th and 95th percentiles of 1.5% and 3.1%, respectively, after four rounds of predistortion. When we transmitted the final predistorted signal OTA, we obtained EVM ranging from 6.0% to 7.4% since the computed predistortion did not account for the added air path. However, after four rounds of predistortion, we obtained EVM ranging from 1.3% to 3.0%. We performed an off-axis OTA measurement as well by keeping the Rx horn antenna at an offset of  $9^\circ$  with respect to the Tx horn antenna. The EVM in this case ranged from 3.4% to 4.5%. In conclusion, we have demonstrated that this modulated-signal source can serve as an important tool for verification and calibration of OTA tests. Further study of the off-axis EVM degradation is planned for future work.

### REFERENCES

- [1] M. Sung *et al.*, "5G trial services demonstration: IFoF-based distributed antenna system in 28 GHz millimeter-wave supporting gigabit mobile services," *J. Lightw. Technol.*, vol. 37, no. 14, pp. 3592–3601, Jul. 15, 2019.
- [2] O. Semiari, W. Saad, M. Bennis, and M. Debbah, "Integrated millimeter wave and sub-6 GHz wireless networks: A roadmap for joint mobile broadband and ultra-reliable low-latency communications," *IEEE Wireless Commun.*, vol. 26, no. 2, pp. 109–115, Apr. 2019.
- [3] G. Zhang *et al.*, "Millimeter-wave channel characterization in large hall scenario at the 10 and 28 GHz bands," in *Proc. 13th Eur. Conf. Antennas Propag. (EuCAP)*, Mar. 2019, pp. 1–4.
- [4] C. Han and S. Duan, "The study on characteristics of rain attenuation along 28 GHz and 38 GHz line-of-sight millimeter-wave links," in *Proc. URSI Asia-Pacific Radio Sci. Conf. (AP-RASC)*, Mar. 2019, pp. 1–3.

- [5] Federal Communications Commission. (Jul. 2016). *Use of Spectrum Bands Above 24 GHz For Mobile Radio Services*. [Online]. Available: <https://www.fcc.gov/document/spectrum-frontiers-ro-and-fnprm>
- [6] *User Equipment (UE) Radio Transmission and Reception; Part 1: Range 1 Standalone (Release 16)*, document 38.101-1; 3GPP, Oct. 2019.
- [7] *User Equipment (UE) Radio Transmission and Reception; Part 2: Range 2 Standalone (Release 16)*, document 38.101-2; 3GPP, Oct. 2019.
- [8] M. R. Palattella *et al.*, "Internet of Things in the 5G era: Enablers, architecture, and business models," *IEEE J. Sel. Areas Commun.*, vol. 34, no. 3, pp. 510–527, Mar. 2016.
- [9] J. Cheng, W. Chen, F. Tao, and C.-L. Lin, "Industrial IoT in 5G environment towards smart manufacturing," *J. Ind. Inf. Integr.*, vol. 10, pp. 10–19, Jun. 2018.
- [10] M. Simsek, A. Aijaz, M. Dohler, J. Sachs, and G. Fettweis, "5G-enabled tactile Internet," *IEEE J. Sel. Areas Commun.*, vol. 34, no. 3, pp. 460–473, Mar. 2016.
- [11] B. Khosravi. *Autonomous Cars Won't Work—Until We Have 5G*. Accessed: Jun. 17, 2019. [Online]. Available: <https://www.forbes.com/sites/bijankhosravi/2018/03/25/autonomous-cars-wont-work-until-we-have-5g/>
- [12] D. M. Pozar, *Microwave Engineering*, 4th ed. Hoboken, NJ, USA: Wiley, Nov. 2011.
- [13] M. Rumney, "Testing 5G: Time to throw away the cables," *Microw. J.*, vol. 59, no. 1, pp. 10–18, Nov. 2016.
- [14] K. A. Remley, D. F. Williams, P. D. Hale, C.-M. Wang, J. Jargon, and Y. Park, "Millimeter-wave modulated-signal and error-vector-magnitude measurement with uncertainty," *IEEE Trans. Microw. Theory Techn.*, vol. 63, no. 5, pp. 1710–1720, May 2015.
- [15] Z. Pi and F. Khan, "An introduction to millimeter-wave mobile broadband systems," *IEEE Commun. Mag.*, vol. 49, no. 6, pp. 101–107, Jun. 2011.
- [16] (Dec. 2015). *FCC Opens 70, 80, and 90 GHz Spectrum Bands for Deployment of Broadband Millimeter Wave Technologies*. [Online]. Available: <https://www.fcc.gov/document/fcc-opens-70-80-and-90-ghz-spectrum-bands-deployment-broadband>
- [17] P. D. Hale, C. M. Wang, D. F. Williams, K. A. Remley, and J. D. Wepman, "Compensation of random and systematic timing errors in sampling oscilloscopes," *IEEE Trans. Instrum. Meas.*, vol. 55, no. 6, pp. 2146–2154, Dec. 2006.
- [18] T. S. Clement, P. D. Hale, D. F. Williams, C. M. Wang, A. Dienstfrey, and D. A. Keenan, "Calibration of sampling oscilloscopes with high-speed photodiodes," *IEEE Trans. Microw. Theory Techn.*, vol. 54, no. 8, pp. 3173–3181, Aug. 2006.
- [19] K. A. Remley, D. F. Williams, P. D. Hale, C. M. Wang, J. A. Jargon, and Y. Park, "Calibrated oscilloscope measurements for system-level characterization of weakly nonlinear sources," in *Proc. Int. Workshop Integr. Nonlinear Microw. Millimetre-Wave Circuits (INMMiC)*, Apr. 2014, pp. 1–4.
- [20] D. F. Williams and A. Lewandowski. (2011). *NIST Microwave Uncertainty Framework*. [Online]. Available: <http://www.nist.gov/ctf/rf-technology/related-software.cfm>
- [21] B. F. Jamroz, D. F. Williams, K. A. Remley, and R. D. Horansky, "Importance of preserving correlations in error-vector-magnitude uncertainty," in *Proc. 91st ARFTG Microw. Meas. Conf. (ARFTG)*, Jun. 2018, pp. 1–4.
- [22] A. J. Weiss *et al.*, "Large-signal network analysis for over-the-air test of up-converting and down-converting phased arrays," in *IEEE MTT-S Int. Microw. Symp. Dig.*, Jun. 2019, pp. 622–625.
- [23] "Understanding AWG7000A series frequency response and DAC performance," Tektronix, Beaverton, OR, USA, Appl. Note 76W-29216-0, 2013.
- [24] "High-speed DACs," Tektronix, Beaverton, OR, USA, Appl. Note 76W-30631-0, 2014.
- [25] *Disclaimer: The Use of Tradenames in This Manuscript is Necessary to Specify Our Methodology and Does Not Imply Endorsement*, Nat. Inst. Standards Technol., Boulder, CO, USA, 2020.
- [26] C. M. J. Wang, P. D. Hale, J. A. Jargon, D. F. Williams, and K. A. Remley, "Sequential estimation of timebase corrections for an arbitrarily long waveform," *IEEE Trans. Instrum. Meas.*, vol. 61, no. 10, pp. 2689–2694, Oct. 2012.
- [27] K. A. Remley, D. F. Williams, D. M. M.-P. Schreurs, G. Loglio, and A. Cidronali, "Phase detrending for measured multisine signals," in *61st ARFTG Conf. Dig.*, Spring 2003, pp. 73–83.
- [28] R. D. Horansky *et al.*, "Comparison of timebase interpolation methods for traceable, wideband mm-wave communication signals," in *Proc. 87th ARFTG Microw. Meas. Conf. (ARFTG)*, May 2016, pp. 1–4.
- [29] P. D. Hale, D. F. Williams, and A. Dienstfrey, "Waveform metrology: Signal measurements in a modulated world," *Metrologia*, vol. 55, no. 5, pp. S135–S151, Oct. 2018.
- [30] Y. Park and K. A. Remley, "Two-stage correction for wideband wireless signal generators with time-interleaved digital-to-analog-converters," in *Proc. 83rd ARFTG Microw. Meas. Conf.*, Jun. 2014, pp. 1–4.
- [31] D. Fry, "Understanding temperature drift in a precision digital-to-analog converter (DAC)," Maxim Integr., San Jose, CA, USA, Appl. Note 4672, 2012. [Online]. Available: <https://www.maximintegrated.com/en/design/technical-documents/app-notes/4/4672.html>
- [32] N. B. Carvalho, K. A. Remley, D. Schreurs, and K. G. Gard, "Multisine signals for wireless system test and design [Application Notes]," *IEEE Microw. Mag.*, vol. 9, no. 3, pp. 122–138, Jun. 2008.
- [33] M. D. Mckinley, K. A. Remley, M. Myslinski, J. S. Kenney, and S. B. Nauwelaers, "EVM calculation for broadband modulated signals," in *64th ARFTG Conf. Dig.*, 2004, pp. 45–52.
- [34] R. A. Shafik, M. S. Rahman, and A. R. Islam, "On the extended relationships among EVM, BER and SNR as performance metrics," in *Proc. Int. Conf. Electr. Comput. Eng.*, Dec. 2006, pp. 408–411.
- [35] H. A. Mahmoud and H. Arslan, "Error vector magnitude to SNR conversion for nondata-aided receivers," *IEEE Trans. Wireless Commun.*, vol. 8, no. 5, pp. 2694–2704, May 2009.
- [36] U. A. Bakshi and A. V. Bakshi, *Antenna and Wave Propagation*. Pune, India: Technical Publications, 2009.
- [37] M. Harper, A. A. Smith, A. Basu, and D. Humphreys, "Calibration of a 70 GHz oscilloscope," in *Proc. Conf. Precis. Electromagn. Meas.*, Jun. 2004, pp. 530–531.
- [38] H. Fuser *et al.*, "Optoelectronic time-domain characterization of a 100 GHz sampling oscilloscope," *Meas. Sci. Technol.*, vol. 23, no. 2, Feb. 2012, Art. no. 025201.
- [39] D. F. Williams, P. D. Hale, T. S. Clement, and J. M. Morgan, "Mismatch corrections for electro-optic sampling systems," in *Proc. 56th ARFTG Conf. Dig.*, Nov. 2000, pp. 1–5.
- [40] D. F. Williams, P. D. Hale, T. S. Clement, and J. M. Morgan, "Calibrating electro-optic sampling systems," in *IEEE MTT-S Int. Microw. Symp. Dig.*, May 2001, pp. 1527–1530.
- [41] D. F. Williams, P. D. Hale, and T. S. Clement. (Dec. 2004). *Uncertainty of the NIST Electrooptic Sampling System*. pp. 1–30. [Online]. Available: <https://www.nist.gov/publications/uncertainty-nist-electrooptic-sampling-system>

**Paritosh Manurkar** received the Ph.D. degree in electrical engineering from Northwestern University, Evanston, IL, USA, in 2016.

In 2016, he joined the University of Colorado (CU) at Boulder, Boulder, CO, USA, as a Post-Doctoral Associate. He has been working with the National Institute of Standards and Technology (NIST), Boulder, as an Associate, through a CU-NIST Partnership. He is currently involved in development of precision, calibrated, and traceable modulated-signal sources at millimeter-wave frequencies and performing traceable over-the-air measurements. He has previously worked on time and frequency transfer between optical clocks, development of fully self-referenced fiber frequency combs, nonlinear optics experiments using shaped pulses, fabrication of infrared detectors, and semiconductor engineering.



**Robert D. Horansky** (Member, IEEE) received the B.A. degree in chemistry and the Ph.D. degree in physics from the University of Colorado at Boulder, Boulder, CO, USA, in 1999 and 2005, respectively. His thesis work focused on low-noise dielectric measurements on novel materials in molecular electronics.

Since 2005, he has been with the National Institute of Standards and Technology (NIST), Boulder, where he started out developing the highest resolving power energy dispersive sensor to date. He then went on to develop metrology techniques for single photon sensors in nuclear radiation and optical power measurements. In 2015, he joined the Metrology for the Wireless Systems Project with the Communications Technology Laboratory, NIST, developing calibrations and traceability for millimeter-wave wireless systems and reverberation-chamber measurements for cellular applications.

Dr. Horansky is the Secretary of the IEEE P1765 Standards Working Group on Uncertainty for EVM.



**Benjamin F. Jamroz** received the Ph.D. degree in applied mathematics from the University of Colorado at Boulder, Boulder, CO, USA, in 2009, where he developed new analytical and numerical models for plasma physics.

As a Computational Scientist, his work includes modeling physical phenomena, including electromagnetics and fluid dynamics and applying machine-learning techniques. In 2017, he joined the Communications Technology Laboratory, National Institute of Standards and Technology, (NIST),

Boulder, where he models and analyzes the complex systems required for high-frequency communications.



**Jeffrey A. Jargon** (Senior Member, IEEE) received the B.S., M.S., and Ph.D. degrees in electrical engineering from the University of Colorado at Boulder, Boulder, CO, USA, in 1990, 1996, and 2003, respectively.

Since 1990, he has been a Staff Member of the National Institute of Standards and Technology (NIST), Boulder, where he has conducted research in the areas of vector network analysis, optical performance monitoring, and waveform metrology. He is currently a member of the High-Speed Measurements Project with the Communications Technology Laboratory, NIST.

He is also a Registered Professional Engineer in the State of Colorado and an ASQ Certified Quality Engineer.

Dr. Jargon was a recipient of four best paper awards, the URSI Young Scientist Award, and the Department of Commerce Silver Medal Award.



**Dylan F. Williams** (Fellow, IEEE) received the Ph.D. degree in electrical engineering from the University of California at Berkeley, Berkeley, CA, USA, in 1986.

In 1989, he joined the Electromagnetic Fields Division, National Institute of Standards and Technology (NIST), Boulder, CO, USA, where he develops electrical waveform and microwave metrology. He has published over 100 technical articles.

Dr. Williams was a recipient of the Department of Commerce Bronze and Silver Medals, the Astin Measurement Science Award, two Electrical Engineering Laboratory's Outstanding Paper Awards, three Automatic RF Techniques Group (ARFTG) Best Paper Awards, the ARFTG Automated Measurements Technology Award, the IEEE Morris E. Leeds Award, the European Microwave Prize, and the 2013 IEEE Joseph F. Keithley Award. He also served as an Editor for the IEEE TRANSACTIONS ON MICROWAVE THEORY AND TECHNIQUES from 2006 to 2010, the Executive Editor for the IEEE TRANSACTIONS ON TERAHERTZ SCIENCE AND TECHNOLOGY, and the 2017 President of the IEEE Microwave Theory and Techniques Society.



**Kate A. Remley** (Fellow, IEEE) received the Ph.D. degree in electrical and computer engineering from Oregon State University, Corvallis, OR, USA, in 1999.

From 1983 to 1992, she was a Broadcast Engineer at Eugene, OR, USA, serving as the Chief Engineer of an AM/FM Broadcast Station from 1989 to 1991. In 1999, she joined the RF Technology Division, National Institute of Standards and Technology (NIST), Boulder, CO, USA, as an Electronics Engineer. She is currently the Leader of the Over-the-Air Metrology Project, NIST, where her research activities include the development of calibrated measurements for microwave and millimeter-wave wireless systems, characterizing the link between nonlinear circuits and system performance, and developing standardized over-the-air test methods for the wireless industry.

Dr. Remley is a member of the Oregon State University Academy of Distinguished Engineers. She was a recipient of the Department of Commerce Bronze and Silver medals and the ARFTG Best Paper Award. She was the Chair of the IEEE Microwave Theory and Techniques Society (MTT-S) Technical Committee on Microwave Measurements from 2008 to 2010, the Editor-in-Chief of the *IEEE Microwave Magazine* from 2009 to 2011, and the Chair of the MTT-S Fellows Evaluation Committee from 2017 to 2018. She was a Distinguished Lecturer of the IEEE Electromagnetic Compatibility Society from 2016 to 2017.

Dr. Remley is a member of the Oregon State University Academy of Distinguished Engineers. She was a recipient of the Department of Commerce Bronze and Silver medals and the ARFTG Best Paper Award. She was the Chair of the IEEE Microwave Theory and Techniques Society (MTT-S) Technical Committee on Microwave Measurements from 2008 to 2010, the Editor-in-Chief of the *IEEE Microwave Magazine* from 2009 to 2011, and the Chair of the MTT-S Fellows Evaluation Committee from 2017 to 2018. She was a Distinguished Lecturer of the IEEE Electromagnetic Compatibility Society from 2016 to 2017.